

Journal of Materials Chemistry C

Accepted Manuscript



This is an *Accepted Manuscript*, which has been through the Royal Society of Chemistry peer review process and has been accepted for publication.

Accepted Manuscripts are published online shortly after acceptance, before technical editing, formatting and proof reading. Using this free service, authors can make their results available to the community, in citable form, before we publish the edited article. We will replace this *Accepted Manuscript* with the edited and formatted *Advance Article* as soon as it is available.

You can find more information about *Accepted Manuscripts* in the [Information for Authors](#).

Please note that technical editing may introduce minor changes to the text and/or graphics, which may alter content. The journal's standard [Terms & Conditions](#) and the [Ethical guidelines](#) still apply. In no event shall the Royal Society of Chemistry be held responsible for any errors or omissions in this *Accepted Manuscript* or any consequences arising from the use of any information it contains.

Unravelling the onset of the exchange bias effect in Ni(core)@NiO(shell) nanoparticles embedded in a mesoporous carbon matrix[†]

Natalia Rinaldi-Montes,^{*a} Pedro Gorria,^b David Martínez-Blanco,^c Zakariae Amghouz,^c Antonio B. Fuertes,^d Luis Fernández Barquín,^e Imanol de Pedro,^e Luca Olivi,^f and Jesús A. Blanco^a

Received Xth XXXXXXXXXXXX 20XX, Accepted Xth XXXXXXXXXXXX 20XX

First published on the web Xth XXXXXXXXXXXX 200X

DOI: 10.1039/b000000x

Ni(core)@NiO(shell) nanoparticles (NPs) were synthesized through the pyrolysis of an inorganic precursor taking place within the pores of an active carbon matrix at different temperatures between 673 and 1173 K, and a subsequent oxidation in air. For the lowest temperature (673 K), the smallest average size of the NPs (9 nm) and the largest percentage of NiO (82%) are observed. Upon increasing the temperature up to 1173 K, an average diameter of 23 nm is estimated while the NiO percentage decreases below 20%. We found that each NP consists of a Ni core surrounded by a structurally disordered NiO shell with a constant thickness of ~ 2 nm, regardless of the core size. The spins inside the NiO shell freeze into a spin glass (SG)-like state below $T_f \sim 40$ K. The magnetic exchange coupling between the Ni core and the NiO shell gives rise to the occurrence of the exchange bias (EB) effect, whose temperature dependence follows a universal exponential trend in all samples. The SG nature of the shell spins yields a vanishing EB above T_f . This is far below the Néel temperature of bulk antiferromagnetic NiO ($T_N \sim 523$ K) that usually determines the onset of the EB effect in Ni/NiO interfaces.

Introduction

The spontaneous formation of a surface oxide layer in transition metal (e.g., Fe, Co, Ni) nanoparticles (NPs) when exposing them to air gives rise to a core@shell morphology that very often modifies the magnetic properties of the system.^{1–3} Transition metal oxides are usually antiferromagnetic (AFM) or ferrimagnetic (FI) and exhibit a considerably lower saturation magnetization (M_S) than their corresponding metals. Therefore, the oxide coating around the metallic core restricts the ferromagnetic (FM) volume of the NP, thus reducing M_S compared to that of the bulk metal.^{4–12} Higher M_S values can be achieved for larger NP sizes, since the thickness of the surface oxide layer does not change appreciably in most of the cases, while the metallic core grows in size and consequently the FM volume does. However, the blocking temperature increases with NP size, even above room temperature, and the

NPs should not behave as superparamagnetic (SPM) entities, thus becoming aggregated.¹⁰ Many efforts have been done in order to produce oxide-free NPs, encapsulated by silica^{13,14} or graphite layers.^{15–21}

The usual procedure followed to obtain metal(core)@oxide(shell) NPs consists of first synthesizing FM NPs by different techniques such as chemical reduction,^{22–24} sol-gel,^{25–28} spray pyrolysis,²⁹ laser ablation,³⁰ thermal decomposition⁹ or high energy ball milling.^{31–33} Afterwards, FM NPs are exposed to air or further processed through reactive treatments in order to create the oxide shell. Habitually, this coating exhibits a high degree of structural disorder that transforms the conventional AFM or FI order displayed by the bulk oxide into a spin glass (SG)-like magnetic state.^{33–35} That conversion has dramatic consequences in the macroscopic magnetic behaviour of the system.^{34,36,37}

The so-called exchange bias (EB) effect manifest as an horizontal shift of the hysteresis loop because of the magnetic exchange interaction at the interface between two magnetic materials, one of them having an anisotropy energy larger than the interface exchange interaction energy between them, typically a FM and an AFM.^{38,39} The effect usually occurs when the system is cooled in a static magnetic field through the Néel temperature (T_N) of the AFM, the Curie temperature of the FM being larger than T_N .⁴⁰ Nevertheless, if the ordered magnetic arrangement of the AFM collapses into a SG state due to size effects, both the magnitude and the onset temperature of the

[†] Electronic Supplementary Information (ESI) available: TEM size distributions and enlarged views and fits to Langevin functions of the room temperature $M(H)$ curves. See DOI: 10.1039/b000000x/

^a Departamento de Física, Universidad de Oviedo, E-33007 Oviedo, Spain. E-mail: nataliarin@gmail.com

^b Departamento de Física & IUTA, EPI, Universidad de Oviedo, E-33203 Gijón, Spain.

^c Servicios Científico-Técnicos, Universidad de Oviedo, E-33006 Oviedo, Spain.

^d Instituto Nacional del Carbón, CSIC, E-33080 Oviedo, Spain.

^e CITIMAC, Facultad de Ciencias, Universidad de Cantabria, E-39005 Santander, Spain.

^f Elettra-Sincrotrone Trieste S.C.p.A., 34149 Basovizza, Trieste, Italy.

EB are drastically reduced.^{33,39}

Among all transition metal NPs, nickel NPs have attracted a great interest due to their wide applications in catalysis^{8,41,42} and bioseparation.^{7,43,44} Together with the reduction of the saturation magnetization, a considerable enhancement of the low-temperature magnetic response has been observed in Ni NPs.^{10,12} Both effects become progressively more important as the size of the particle is reduced due to the higher surface-to-volume ratio. Different explanations have been proposed in order to account for those changes in the magnetic behaviour, *e.g.* the oxidation of Ni,^{8,45} the partially amorphous structure of the NPs¹⁰ and the existence of a magnetic dead layer.⁴⁶ In addition, it has been reported that the EB effect in Ni@NiO NPs vanishes below the expected T_N of AFM NiO ($T_N \sim 523$ K).³³ To understand the underlying cause of this EB reduction at the nanoscale still remains an open question whose interest lies in the crucial role that Ni/NiO junctions play as stabilizing elements in spin valves and tunneling devices.⁴⁷

In order to contribute to elucidate the above mentioned controversies, we have investigated a series of Ni@NiO NPs with average sizes of 9, 10, 11, 16 and 23 nm. We used a one-pot pyrolysis reaction to embed the NPs inside the pores of an active carbon matrix, thus avoiding particle aggregation. Then, an oxidation in air allowed the formation of a NiO shell at the NP surface. A joint analysis combining x-ray powder diffraction, high resolution transmission electron microscopy and x-ray absorption spectroscopy with exhaustive magnetic measurements unravels the key role of the surface NiO shell in the macroscopic magnetic behaviour of the Ni@NiO NPs. In particular, the coupling mechanism at the Ni/NiO interface leading to a low-temperature vanishing EB effect will be discussed in detail.

Experimental

Materials synthesis

A commercial activated carbon (AC) was employed as a nanotemplate for the synthesis of Ni@NiO NPs. The AC material, supplied by Osaka Gas (Japan), has a large Brunauer-Emmett-Teller (BET) surface area of $2350 \text{ m}^2 \cdot \text{g}^{-1}$, a high pore volume of $1.47 \text{ cm}^3 \cdot \text{g}^{-1}$ and a porosity made up of mesopores of up to 6–7 nm diameter (~ 2.5 nm in average). The synthetic method is based on a pyrolysis process taking place within the restricted volume formed by the AC porosity.

In a typical fabrication procedure, 1 g of AC was impregnated with a solution formed by 1 g nickel (II) nitrate hexahydrate in 4 mL of ethanol. The impregnated sample was vacuum-dried at 323 K for several hours and subsequently heat-treated in a N_2 atmosphere at a selected temperature (T_H) for 3 hours. Under these conditions, the decomposition of the Ni precursor into NiO took place first. Subsequently, upon in-

creasing temperature, NiO was reduced by means of carbon ($2 \cdot \text{NiO} + \text{C} \rightarrow 2 \cdot \text{Ni} + \text{CO}_2$) and Ni atoms nucleated forming NPs according to Ostwald ripening phenomenon. This nucleation process is thermodynamically driven by the balance between the surface and volume contributions to the free energy of the NPs.⁴⁸ Therefore, T_H constitutes a key parameter that enables the control of the NP average diameter; the larger the T_H , the bigger the size is. Finally, the sample was cooled under nitrogen down to room temperature and then passivated with a small stream of air to stabilize it, so that the action of atmospheric O_2 oxidizes the surface layers into NiO. The NPs resulting from the above process were formed by a Ni core surrounded by a NiO shell (Ni@NiO). Five different samples were synthesized at 673, 773, 873, 1023 and 1173 K and labeled as T673, T773, T873, T1023 and T1173, respectively. The Ni content was $\sim 11 \text{ wt}\%$ in all the samples as deduced from thermo-gravimetric analysis (TGA).

Structural and microstructural characterization

Transmission electron microscopy (TEM and HRTEM) images were recorded on JEOL2000-EXII and JEOL-JEM-2100F microscopes (200 kV), respectively. Samples were prepared by depositing a small amount of powder in ethanol and then by placing several drops of this solution on carbon films, which were set on copper grids. In order to determine the distribution size of each sample, around 10000 NPs were counted, using the PSA macro for ImageJ,⁴⁹ and modeled with a lognormal fit.

The crystalline structure of the samples was determined from room temperature x-ray powder diffraction (XRD). The patterns were collected by means of a Philips X'Pert PRO MPD diffractometer operating at 45 kV and 40 mA, using a Cu anode ($\lambda = 1.5406 \text{ \AA}$) and equipped with a germanium Johansson monochromator and a PIXcel solid angle detector. The full profile analysis of the diffraction patterns was performed using the FullProf suite package⁵⁰ based on the Rietveld method,⁵¹ with rather good reliability factors, *i.e.*, the R-weighted pattern (R_{wp}) was below 10%, in all the cases.

The near-edge (XANES) region of the x-ray absorption fine structure (XAFS) spectrum extends $\sim 50 \text{ \AA}$ from the absorption edge (E_0). It contains information about the valence state and to the chemical coordination of the absorbing atom. The room temperature Ni *K*-edge XANES spectra of the samples together with those of Ni and NiO bulk standards were measured in transmission mode on the XAS beamline at the Elettra Sincrotrone Trieste (Italy) using standard ionization chambers for the intensity detection. In order to calibrate the energy, the spectrum of a Ni metal reference was recorded together with that of the sample. The preparation of the samples consisted of homogeneous layers of powder spread over an adhesive Kapton tape. The thickness and homogeneity of the sam-

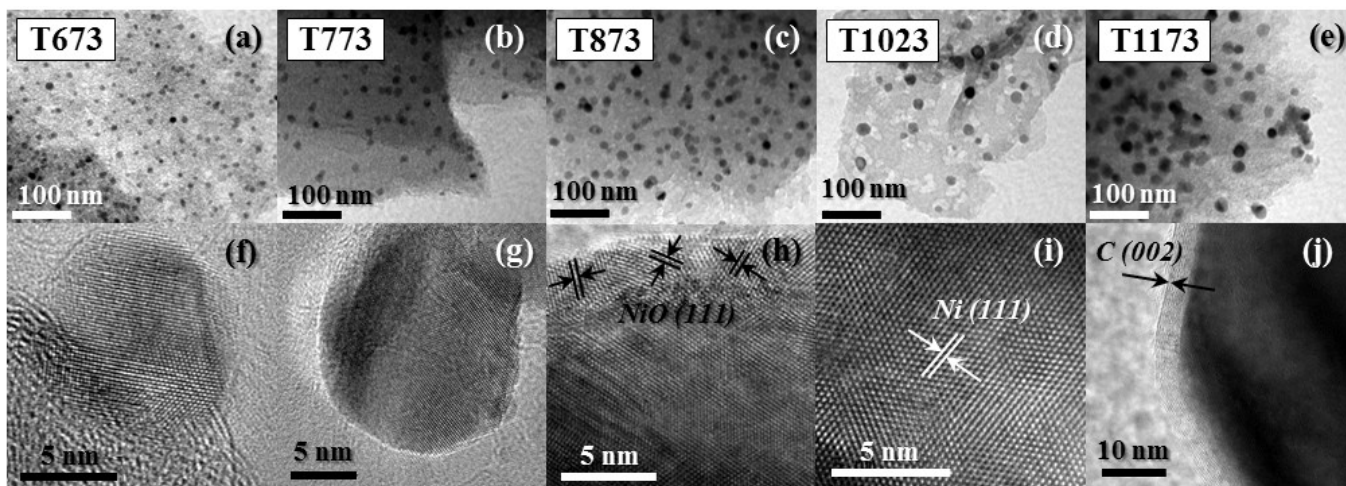


Fig. 1 (Color online) (a-e) TEM images for samples (a) T673, (b) T773, (c) T873, (d) T1023 and (e) T1173. (f-g) HRTEM images of individual NPs. (h-j) Interplanar distances of (h) NiO(111), (i) Ni(111) and (j) C(002).

ples were optimized to obtain the best signal-to-noise ratio. The analysis of the absorption spectra, including data reduction, background removal and normalization was carried out using Athena package.⁵²

Magnetometry

The temperature and magnetic field dependences of the magnetization, $M(T)$ and $M(H)$ curves, were measured in a Quantum Design PPMS-9T platform equipped with a vibrating sample magnetometer (VSM) option. First, the sample was cooled in zero-field (ZFC) from 325 K down to 5 K. Then a constant magnetic field was applied and the $M_{ZFC}(T)$ curve was measured on heating from 5 K to 325 K. After reaching the highest temperature (325 K), and maintaining the magnetic field constant, the field cooling (FC) magnetization *vs.* temperature, $M_{FC}(T)$, curve was recorded on cooling the sample from 325 K down to 5 K. The $M(H)$ loops were measured between -85 and 85 kOe at low (5 K) and room (300 K) temperatures. As a complement to the above measurements, a MicroSense VSM (EV9 series) magnetometer was used in order to determine with high accuracy the coercive field and remanent magnetization of the samples at $T = 300$ K. It is worth noting that the magnetic signal of the active carbon template is diamagnetic. It was measured separately, the magnetic signal being two orders of magnitude lower than that coming from the NPs; hence, we consider it negligible. Therefore, the recorded signal of the samples was normalised to the total mass of Ni taking into account the Ni percentage in the sample obtained from TGA, and, in all cases, the magnetization is expressed in emu per gram of Ni ($\text{emu} \cdot \text{g}^{-1}\text{Ni}$).

In order to investigate the EB effect in this Ni@NiO system,

each sample was cooled down from 300 down to 5 K under a constant applied magnetic field (H_{cool}). After that, a hysteresis loop was recorded between -50 and 50 kOe at $T = 5$ K. The EB field (H_{EB}) is defined as the horizontal shift of the central point of the loop measured under a given H_{cool} , relative to that measured under $H_{cool} = 0$ loop, *i.e.*, $H_{EB} = -(H_{C1} + H_{C2})/2$, where H_{C1} and H_{C2} are the left and right coercive fields, respectively.

Results and discussion

Microstructure and morphology

Transmission electron microscopy. Figs. 1a-e show representative TEM images of the five samples where individual, well-dispersed and quasi-spherical NPs can be identified. In fact, the carbonaceous matrix is formed by micrometric grains, each one of them having a sponge-like morphology with numerous interconnected pores at the submicron length scale. During the synthesis procedure, the NPs grow at the intersections of the AC matrix pores. Let us go now deeper into a single NP by examining the HRTEM images at the second row of Fig. 1 (Figs. 1f-j). Although the dissimilarity between Ni and NiO is not easy to perceive due to a feeble atomic contrast and same crystal structure, the crossover from one phase to another is more or less self-evident when the interplanar distance (d) is measured. Thereby, $d \sim 2.0$ Å [$= d_{Ni}^{(111)}$] in the core part of the NP (Fig. 1i) and it increases up to $d \sim 2.4$ Å [$= d_{NiO}^{(111)}$] as we approach the edge (Fig. 1h). In addition, local EDX (energy-dispersive x-ray spectroscopy) measurements on different NPs give an atomic composition of about 60% Ni + 40% O near the NP edge, while only Ni is present in the core

Table 1 Parameters obtained from the structural and magnetic characterization of the samples (see text for details).

			T673	T773	T873	T1023	T1173
TEM (Lognormal fit)		$D_{TEM}(\sigma)$ (nm)	9(5)	10(4)	11(4)	16(6)	23(14)
XRD		D_{Ni}^{XRD} (nm)	6(2)	7(2)	9(2)	13(5)	20(10)
XANES		X_{Ni} (%)	18(5)	26(5)	36(6)	66(4)	83(5)
		X_{NiO} (%)	82(5)	74(5)	64(6)	34(4)	17(5)
$M(H)$ curves	$T = 300$ K	M_S (emu·g ⁻¹ Ni)	4.6(1)	8.0(1)	12.2(1)	28.4(1)	40.3(1)
	$T = 5$ K	H_C (Oe)	642(1)	631(1)	564(1)	521(1)	416(1)
		M_r (emu·g ⁻¹ Ni)	2.6(1)	4.2(1)	6.3(1)	13.1(1)	20.5(1)

region of the NP. Therefore, the above hints allow us to estimate the thickness of the NiO shell to be ~ 2 nm, irrespective of the NP size. As far as the microscopic arrangement inside each NP is concerned, Fig. 1i offers clear evidence that the Ni core is single crystalline and has no crystallographic defects. By contrast, the NiO shell is composed of very small and randomly oriented nanocrystallites within which atomic vacancies and dislocations can be discerned (Fig. 1h). This can be understood in terms of the slow nucleation of the Ni cores at high temperature ($T_H > 673$ K) compared to the fast growth of the structurally disordered NiO surface shell due to air oxidation at room temperature.

From the NP size histogram and the fit to a lognormal distribution of each sample (Fig. S1 in Supplementary Information), we have estimated also the average value for the NP diameter (D_{TEM}) and the standard deviation (σ). Those values increase from $D_{TEM}(\sigma) = 9(5)$ to $23(14)$ nm for samples T673 and T1173, respectively (see Table 1), telling us that the temperature of the synthesis, T_H , plays a crucial role in the NP size distribution. It is worth noting that D_{TEM} corresponds to the size of the NP as a whole entity, *i.e.*, including the Ni core diameter and the NiO shell thickness.

X-ray powder diffraction. The experimental and calculated XRD patterns corresponding to the five samples are depicted in Fig. 2. Three different crystallographic phases were included in order to properly fit whole patterns. Ni and NiO (with face centered cubic and rocksalt $Fm\bar{3}m$ crystal structures, respectively) as being the NP constituents, and graphite (space group $P 6_3/mmc$) coming from the AC matrix. The values for the lattice parameter of the crystalline Ni core and NiO shell [$a_{Ni} = 3.52(1)$ and $a_{NiO} = 4.17(1)$ Å] do not vary appreciably, within the estimated error, in the five samples and match with those already reported in bulk materials (3.520 and 4.178 Å, for Ni and NiO respectively).^{43,53} However, the diffraction peaks corresponding to the Ni core become narrower upon increasing the value of T_H during the synthesis procedure, thus suggesting a larger average size for the NPs as confirmed from HRTEM images (see previous subsection). Similarly, those diffraction peaks corresponding to the graphite Bragg reflections exhibit a significant sharpening, but

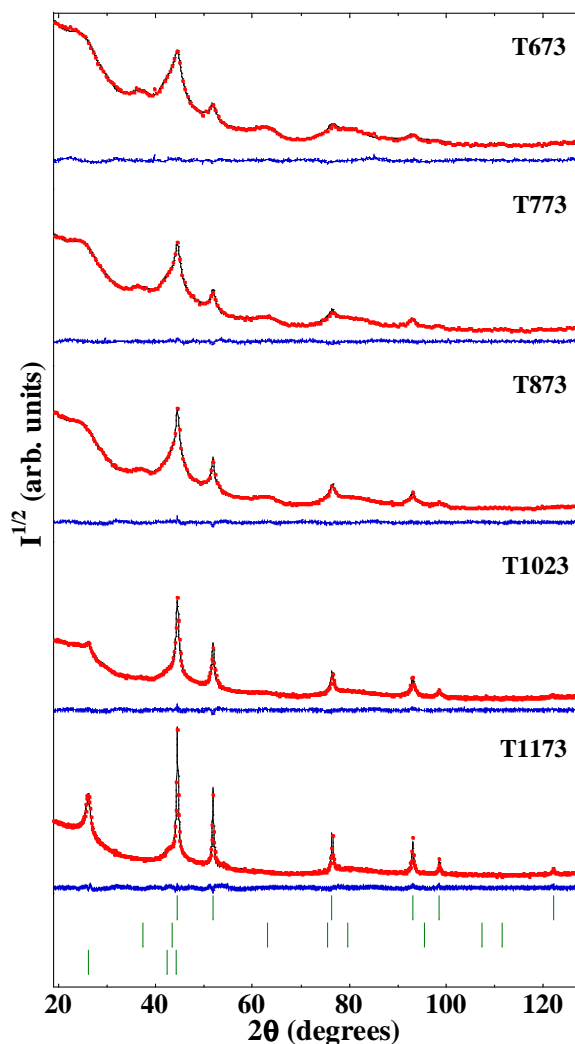


Fig. 2 (Color online) Room temperature XRD patterns of the samples, displayed in square root scale. Points (solid-lines) are the observed counts (calculated Rietveld refinements). The curve at the bottom of each figure is the difference pattern given by $I_{obs} - I_{cal}$. The small vertical marks indicate the angular positions of the allowed Bragg positions of the Ni (top), NiO (middle) and graphite (bottom) crystallographic phases.

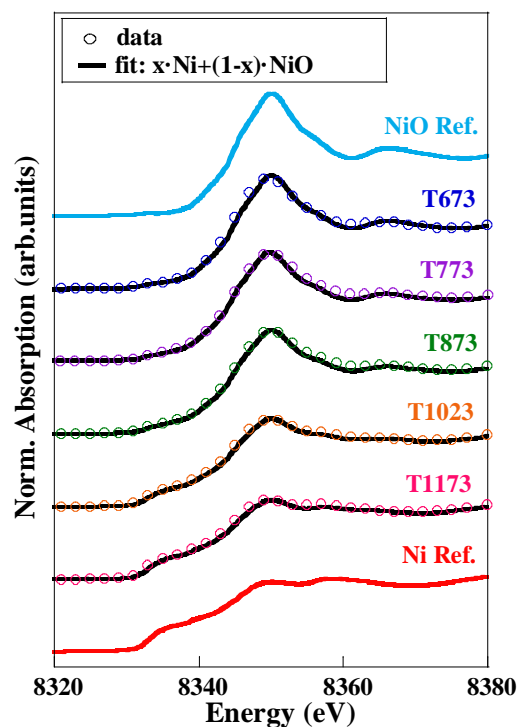


Fig. 3 (Color online) Room temperature XANES spectra of the samples (empty circles), together with Ni and NiO bulk standards. Lines represent the best fits of the data to weighted combinations of Ni and NiO, calculated by the method of least squares (see text for details).

in this case, this fact might be ascribed to the local graphitization of the amorphous AC matrix promoted by the presence of NPs. In fact, Ni NPs have been reported to be excellent catalysts for the growth of carbon nanotubes (see Fig. 1j).^{54,55} Let us focus now on the variation of the average NP diameter as the temperature T_H is changed. In Table 1 we notice that the average crystallite size for the Ni core (D_{Ni}^{XRD}) slightly increases (from 6 to 9 nm) between the lowest value of T_H (673 K) and $T_H = 873$ K. However, the increase is more pronounced for the two higher synthesis temperatures, reaching a value of $D_{Ni}^{XRD} = 30$ nm at $T_H = 1173$ K. On the contrary, the average size of the NiO crystalline contribution, that we have to consider as the thickness of the shell (t_{NiO}^{XRD}) instead of a true diameter, remains almost constant at around 1.9 nm for all the samples. It is worth to highlight that the NP diameter values obtained from XRD analysis, $D^{XRD} = D_{Ni}^{XRD} + (2 \times t_{NiO}^{XRD})$, correspond very closely to the values estimated from the TEM images (see Table 1).

X-ray absorption spectroscopy. Fig. 3 displays the room temperature XANES spectra of the five samples, measured at the Ni K -edge ($E_0 \sim 8333$ eV), together with those of Ni and NiO bulk standards. According to XRD results only two

substances containing Ni atoms have been detected within the samples, namely metallic Ni and nickel monoxide (NiO). The unlike oxidation state of nickel atoms in metallic Ni (Ni^0 valence) with respect to NiO (Ni^{2+} valence), is easy to recognize in their corresponding XANES spectra that display characteristic and distinctive features (Fig. 3). We therefore have modeled the experimental XANES spectra of the five samples by means of a weighted combination of the contributions coming from nickel absorbers in both Ni core and NiO shell regions of the NPs. The best fit, after applying a least squares procedure, gives us the relative percentage of Ni atoms in each phase (X_{Ni} , X_{NiO}) (see Table 1). We note that the relative percentage of NiO increases dramatically when reducing NP size. This finding can be easily understood taking into account that the oxidation due to air exposition involves the external part of the NP, and due to a higher surface to volume ratio the percentage of oxidized Ni atoms is significantly higher in smaller NPs. Based on geometric arguments and assuming that D_{TEM} is the diameter of the entire NP, we use Eq. 1 in order to estimate the thickness of the NiO shell (t_{NiO}):

$$t_{NiO} = \frac{D_{TEM}}{2} \left\{ 1 - \left[\left(\frac{X_{NiO} \rho_{Ni}}{X_{Ni} \rho_{NiO}} \right) + 1 \right]^{-1/3} \right\} \quad (1)$$

where, ρ_{Ni} and ρ_{NiO} are the densities of Ni and NiO phases, respectively ($\rho_{Ni} = 4/a_{Ni}^3$, $\rho_{NiO} = 4/a_{NiO}^3$). The resulting thickness is around 2 nm for all the samples, in good agreement with the values obtained from XRD and TEM analysis (see Table 1).

Magnetic behaviour

Fig. 4 shows the evolution of the magnetization as a function of temperature under a magnetic field of $H = 50$ Oe for samples T673, T873 and T1173. Two sets of curves are depicted for each sample (Figs. 4a-c): (i) those corresponding to the measurements performed on heating after zero-field-cooling, $M_{ZFC}(T)$ curves (in blue); and (ii) the data obtained during field-cooling, $M_{FC}(T)$ curves (in red). All samples exhibit typical features of single domain ferromagnetic NPs that remain blocked below a certain temperature (T_B , blocking temperature) and behave as superparamagnets for $T > T_B$. The temperature at which the $M_{ZFC}(T)$ curve shows a maximum is usually ascribed to the mean T_B of the system (*i.e.* $T_B \sim 80$ K for sample T673, see Fig. 4a). Nonetheless, an increase of the NP average size provokes a shift of T_B towards higher temperatures. In addition, if the NP size distribution broadens, the maximum of the $M_{ZFC}(T)$ curve becomes poorly defined, since the NPs enter into the SPM regime at a wider interval of temperatures depending on their size (Figs. 4b and c). In the case of samples T1023 and T1173, the splitting of the $M_{ZFC}(T)$ and $M_{FC}(T)$ curves up to $T = 325$ K (Fig. 4c)

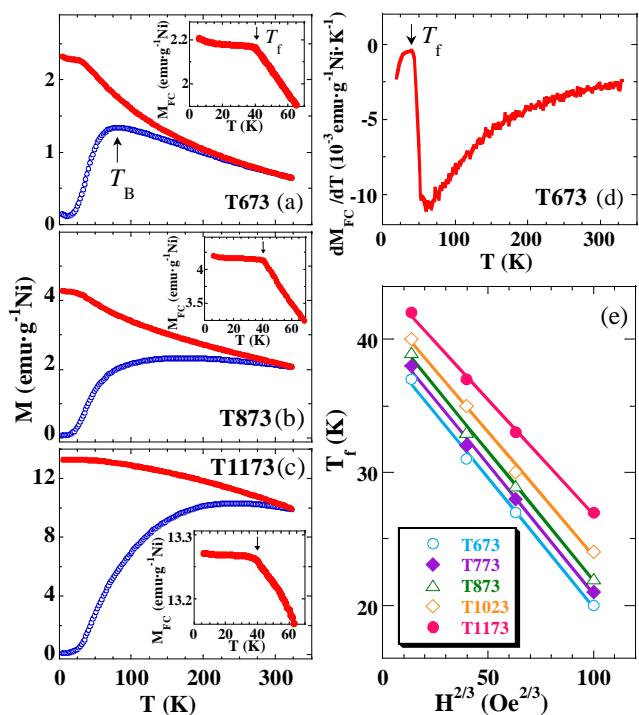


Fig. 4 (Color online) ZFC (blue squares) and FC (red circles) magnetization curves measured for samples (a) T673, (b) T873 and (c) T1173, under a magnetic field of 50 Oe. Insets in (a-c) show enlarged portions of the $M_{FC}(T)$ curves. (d) Temperature derivative of the $M_{FC}(T)$ curve for sample T673. (e) Fits of T_f vs. $H^{2/3}$ to de Almeida-Thouless lines for all samples (see text for details).

indicates that the spins inside the largest NPs in the size distribution of these samples (see Fig. S1 in Supplementary Information) are still in a blocked magnetic state at $T = 325$ K.

On the other hand, it is interesting to note that all samples present a kink in the $M_{FC}(T)$ curve at $T_f \sim 40$ K (see insets in Figs. 4a-c), manifested as a sharp increase in the temperature derivative of $M_{FC}(T)$ (Fig. 4d). We additionally measured the $M_{FC}(T)$ curves under several values of the magnetic field (H) up to 1 kOe and we found that T_f decreases linearly with $H^{2/3}$ (Fig. 4e). This dependence corresponds to the so-called de Almeida-Thouless line, which is viewed as a hint for the presence of a SG phase in the system.^{56,57} Hence, a SG-like freezing seems to be taking place inside our system at $T_f \sim 40$ K. In addition, for sample T673 a tiny increase of the magnetization occurs in both $M_{ZFC}(T)$ and $M_{FC}(T)$ curves below $T = 10$ K (Fig. 4a). A similar feature has also been reported in γ -Fe₂O₃ and Fe@ γ -Fe₂O₃ NPs, being attributed to the onset of the freezing process of disordered surface spins.^{35,58} This explanation is in good agreement with the fact that sample T673 presents the smallest average size and thus the highest surface-to-volume ratio.

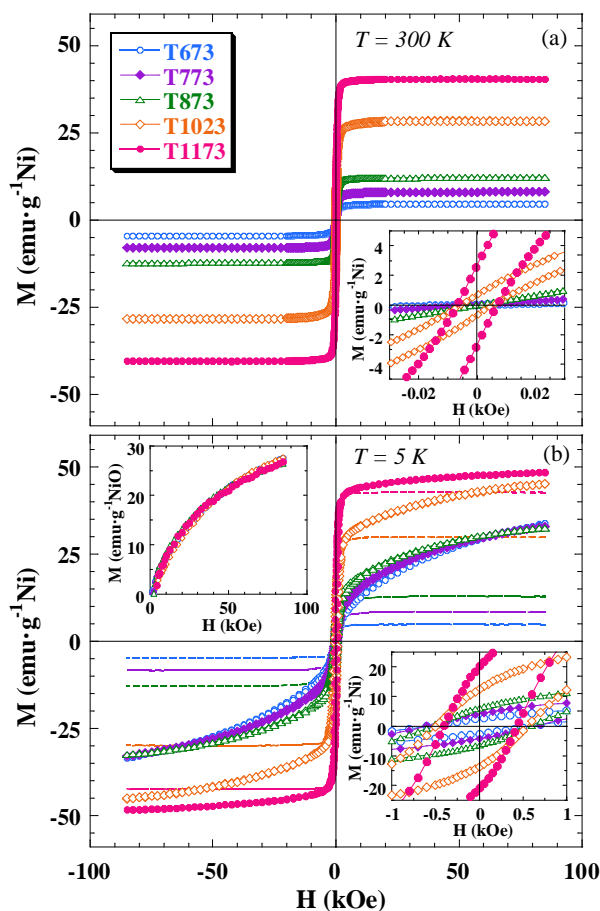


Fig. 5 (Color online) $M(H)$ curves of the samples measured in ZFC conditions at (a) $T = 300$ K and (b) $T = 5$ K. Lower right insets show an enlarged view of the central part of the loops. Upper left inset in (b) contains the magnetic signal at $T = 5$ K of the disordered NiO shell, normalized to the NiO mass (see text for details).

In order to study the response of the magnetization to the applied magnetic field, we have measured the $M(H)$ curves within ± 85 kOe range at two selected temperatures: 5 and 300 K (Fig. 5). At $T = 300$ K an almost saturated magnetic signal is observed for $H > 10$ kOe (see Fig. 5a and Table 1), although huge differences in the value of the saturation magnetization (M_S) can be perceived between samples, even if all values lie well below the M_S of bulk Ni ($M_S^{bulk} = 55$ emu·g⁻¹Ni at $T = 300$ K).⁵⁹ The significant reduction in the value of M_S for samples T673, T773 and T873 is a direct consequence of the smaller ratio between metallic and oxidized Ni atoms as the NP size diminishes (see XANES results). The room temperature $M(H)$ curves for samples T673, T773 and T873 (see inset in Fig. 5a and Fig. S2 in Supplementary Information) are reversible, with zero values for both coercive field (H_C) and remanent magnetization (M_r), which is typical of an

assembly of SPM NPs. In addition, the fitting of the $M(H)$ curves with a combination of the Langevin function and the lognormal size distribution⁶⁰ (Fig. S2 in Supplementary Information) provides values for the average size of the Ni cores and the standard deviation that coincide with those obtained from XRD results (see Table 1). In contrast, a small hysteresis loop at room temperature is found for samples T1023 and T1173 ($H_C = 5$ and 7 Oe, $M_r = 0.67$ and $2.70 \text{ emu}\cdot\text{g}^{-1}\text{Ni}$, respectively, see inset in Fig. 5a and Fig. S3 in Supplementary Information), as expected from the splitting of the $M_{ZFC}(T)$ and $M_{FC}(T)$ curves up to $T = 325$ K (Fig. 4c). On the other hand, the low temperature $M(H)$ loops for all samples (Fig. 5b) display non-saturating values of the magnetization, this feature being more remarkable in the case of the samples with smaller NP average size, and non-zero values for H_C and M_r (see the inset in Fig. 5b and Table 1). The hysteretic behaviour of the samples at $T = 5$ K is related to the blocked state of the Ni core spins. Indeed, the value of M_r increases with NP size (see Table 1) as the percentage of metallic Ni does. Conversely, the value of H_C is higher in small NPs (sample T673) compared to larger ones (sample T1173) due to the interfacial magnetic anisotropy exerted by the NiO shell spins on the Ni core ones (see below).

To explain the non-saturating $M(H)$ loops at $T = 5$ K and the larger values of M for $H > 20$ kOe compared with those measured at 300 K (especially in the samples T673, T773 and T873) it is not enough to consider just the temperature variation of the magnetization of pure nickel [$M_S(300 \text{ K}) \sim 55 \text{ emu/g}$ and increases to 58 emu/g at $T = 5$ K, roughly 6%]. Notice that we have plotted in Fig. 5b (dotted lines) the estimated loops corresponding to the Ni core in each sample. Thus, we need to consider two different contributions for the $M(H)$ loops, one coming from the Ni metallic cores, which tends to saturate at low fields, and another one which does not saturate up to 85 kOe. Given that the temperature at which this latter contribution vanishes (the loops look practically saturated) roughly coincides with the freezing temperature estimated from the $M_{FC}(T)$ curves, and that the magnitude of the non-saturating magnetization is much more pronounced in samples with higher percentages of NiO, it seems reasonable to attribute this signal to the surface NiO spins, which are in a SG state below $T_f \sim 40$ K. Going beyond this hypothesis, if we plot the non-saturating magnetization, normalized by the percentage of NiO extracted from XANES analysis, the curves extracted from all samples overlap in the whole range of magnetic field (see upper inset in Fig. 5b), indicating the plausibility of the argument. In this regard, it should be noted that although bulk NiO is AFM with a Néel temperature of $T_N = 523$ K, in a recent study we have reported that this AFM character breaks down within the nanometer length-scale due to uncompensated spin configuration, that gives rise to a net magnetization (up to 60 emu/g for $H = 85$ kOe) and a SG-

like behaviour at low temperatures.³⁶ In the present case, both the thinness of the NiO shell (~ 2 nm) and the presence of a certain structural disorder (see HRTEM results) can be the source of the magnetic frustration leading to the appearance of a SG-like state in the NiO surface spins.

The above hints suggest that each NP can be described as consisting of a metallic Ni core, whose spins transit from the blocked to the SPM regime above T_B , surrounded by a NiO shell in which the spins freeze in a SG-like state below $T_f \sim 40$ K. An additional evidence for this magnetic scenario is given by the $M(H)$ loops measured at $T = 5$ K after cooling the sample from 300 K down to 5 K under a constant applied magnetic field $H_{cool} = 5$ kOe. Fig. 6a shows the $M(H)$ loops of sample T673 measured at $T = 5$ K for $H_{cool} = 0$ and 5 kOe. The loop corresponding to the field-cooled sample is shifted towards the negative H-axis (H_{EB}), exhibiting what is commonly known as EB effect.

As a result, it is reasonable to consider that, in case of an FM-Ni/AFM-NiO configuration, the NiO shell spins should exert a magnetic exchange coupling on the Ni core ones. However, we could expect that the EB effect should survive up to temperatures close to 500 K (just below the T_N of NiO). However, what we observe is that the effect disappears right above $T_f \sim 40$ K (Fig. 6b) This onset temperature is one order of magnitude lower than the values reported to date in Ni@NiO NPs,^{32,33,61} thus indicating that this low-temperature EB in our Ni(core)/NiO(shell) nanoparticulated system has to be rather attributed to a FM-Ni/SG-NiO interface.

We now turn to examine in more detail the EB in these Ni(core)@NiO(shell) NPs. All the samples exhibit the characteristic features of the EB phenomenon (Fig. 6b), although the magnitude of the loop shift (H_{EB}) is more pronounced in the sample with smallest NPs (T673) due to the higher shell-to-core volume ratio. The question remaining relates to understand the temperature evolution of the EB mechanism. Fig. 6b shows an exponential (negative) dependence of HEB with temperature in three samples, and given by

$$H_{EB}(T) = H_{EB}^0 \exp(-T/T_0) \quad (2)$$

where H_{EB}^0 is the extrapolation of H_{EB} at $T = 0$ K and T_0 is a constant. The best fits to Eq. 2 provide values for H_{EB}^0 of 618(32), 386(23) and 105(5) Oe for T673, T873 and T1173, respectively, and a common value of 9.7(6) K for T_0 . This exponential decay of H_{EB} has been already observed in multilayered systems containing amorphous or SG layers and is attributed to magnetic frustration.^{62,63} Moreover, if we plot the normalized EB shift, H_{EB}/H_{EB}^0 , as a function of temperature the curves scale in the whole temperature range (see inset in Fig. 6b). Starting from the latter, a straightforward conclusion can be drawn: the mechanism of magnetic coupling at the Ni/NiO interface must be the same for all the samples. Therefore, we suggest here the following explanation for the

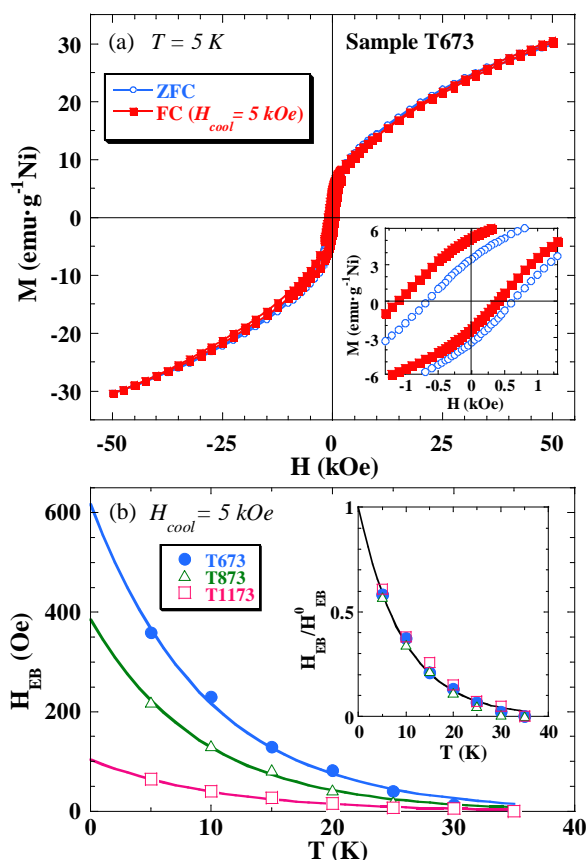


Fig. 6 (Color online) (a) Magnetic hysteresis loops for sample T673 measured at $T = 5$ K after cooling the samples down from $T = 300$ K both in ZFC (solid red squares) and FC [$H_{cool} = 5$ kOe] (empty blue circles) conditions. Inset displays an enlarged view of the central part of the loops, evidencing the occurrence of the EB effect. (b) Temperature variation of H_{EB} (symbols), together with exponential fits (solid lines), for samples T673 (solid blue circles), T873 (empty green triangles) and T1173 (empty red squares). Inset shows the superposition of the normalized H_{EB}/H_{EB}^0 curves.

existence of a low-temperature EB effect. In the presence of an applied magnetic field, the FM Ni core spins aligns parallel to the field direction during the cooling process from $T > T_B$ down to $T_f < T < T_B$, while the magnetically disordered NiO spins thermally fluctuate. Further cooling below T_f provokes the SG freezing of the NiO spins along specific directions driven by the exchange coupling between them and the adjacent core spins at the core/shell interface region. In these conditions, if the direction of the applied magnetic field is reverted below T_f , the SG spins at the interface will exert a microscopic torque on the FM core, trying to keep them in their original direction.

The present findings may be useful for understanding the existence of a low-temperature exchange bias effect in other

metal(core)@oxide(shell) nanoparticulated systems characterized by a structurally disordered shell that, rather than being AFM, behave as a SG-like system due to its reduced dimensionality and to the presence of crystallographic defects.

Conclusions

A series of Ni(core)@NiO(shell) nanoparticles with average sizes ranging from 9 to 23 nm has been prepared by means of the pyrolysis of a Ni salt at different temperatures, followed by an oxidation in air. The microstructure of each nanoparticle can be described as consisting of a metallic Ni core surrounded by a NiO shell with common features in all samples, regardless of the core size. Thus, the shell is formed by small NiO crystallites whose low dimensionality and structural disorder are responsible for a spin glass-like freezing at $T_f \sim 40$ K, far below the Néel temperature of bulk antiferromagnetic NiO ($T_N \sim 523$ K). This highly anisotropic low-temperature state is further evidenced by the reversible and non-saturating shape of the $M(H)$ curve corresponding to the NiO component, which reaches up to $M \sim 30$ $\text{emu}\cdot\text{g}^{-1}\text{NiO}$ at $H = 85$ kOe and $T = 5$ K.

The magnetic exchange coupling at the interface between the metallic Ni core and the magnetically disordered NiO shell gives rise to the appearance of the exchange bias effect. This effect becomes more pronounced in smallest nanoparticles due to their higher interface-to-volume ratio. Nevertheless, the exponential decay of the exchange bias with rising temperature, which is a clear footprint of the magnetic frustration inside the spin glass shell, is universally scalable for all samples. Finally, the temperature at which the exchange bias effect vanishes coincides with the estimated freezing temperature of the NiO phase. This seems to indicate that the onset of the exchange bias effect in air-oxidized Ni@NiO nanoparticles is mainly driven by the properties of the magnetically disordered NiO shell, and less dependent on the size of the metallic Ni core.

Acknowledgements

N. Rinaldi-Montes is grateful to the Spanish Ministerio de Educación, Cultura y Deporte (MECD) for PhD grant with reference FPU12/03381. This work was financially supported by research projects MAT2011-27573-C04 (MINECO, Spain) and FC-15-GRUPIN14-037 (Asturias Government, Spain). We thank Dr. Beatriz Vallina for technical assistance at the SCT's Univ. Oviedo and Elettra-Sincrotrone Trieste (Italy) for allocating beam time (proposal number 20120269).

References

- 1 S. Gangopadhyay, H. Hadjipanayis, B. Dale, C. Sorensen, K. Klabunde, V. Papaefthymiou and A. Kostikas, *Phys. Rev. B*, 1992, **45**, 9778.
- 2 R. G. Chaudhuri and S. Paria, *Chem. Rev.*, 2012, **112**, 2373.
- 3 M. P. Fernandez-Garcia, P. Gorria, J. A. Blanco, A. B. Fuertes, M. Sevilla, R. Boada, J. Chaboy, D. Schmool and J. M. Greneche, *Phys. Rev. B*, 2010, **81**, 094418.
- 4 S. Kar and V. Singh, *J. Alloys Compd.*, 2011, **509**, 3582.
- 5 A. Kremenovic, B. Jancar, M. Ristic, M. Vucinic-Vasic, J. Rogan, A. Pacevski and B. Antic, *J. Phys. Chem. C*, 2012, **116**, 4356.
- 6 B. B. Nayak, S. Vitta, A. K. Nigam and D. Bahadur, *Thin Solid Films*, 2006, **505**, 109.
- 7 I. S. Lee, N. Lee, J. Park, B. H. Kim, Y. W. Yi, T. Kim, T. K. Kim, I. H. Lee, S. R. Paik and T. Hyeon, *J. Am. Chem. Soc.*, 2006, **128**, 10658.
- 8 J. Park, E. Kang, S. U. Son, H. M. Park, M. K. Lee, J. Kim, K. W. Kim, H. J. Noh, J. H. Park, C. J. Bae, J. G. Park and T. Hyeon, *Adv. Mater.*, 2005, **17**, 429.
- 9 M. A. Khadar, V. Biju and A. Inoue, *Mater. Res. Bull.*, 2003, **38**, 1341.
- 10 S. Carencio, C. Boissiere, L. Nicole, C. Sanchez, P. L. Floch and N. Mezaillies, *Chem. Mat.*, 2010, **22**, 1340.
- 11 T. Bala, R. D. Gunning, M. Venkatesan, J. F. Godsell, S. Roy and K. M. Ryan, *Nanotechnology*, 2009, **20**, 415603.
- 12 A. P. LaGrow, B. Ingham, S. Cheong, G. V. M. Williams, C. Dotzler, M. F. Toney, D. A. Jefferson, E. C. Corbos, P. T. Bishop, J. Cookson and R. D. Tilley, *J. Am. Chem. Soc.*, 2012, **134**, 855.
- 13 W. R. Zhao, J. L. Gu, L. X. Zhang, H. R. Chen and J. L. Shi, *J. Am. Chem. Soc.*, 2005, **127**, 8916.
- 14 Y. Deng, D. Qi, C. Deng, X. Zhang and D. Zhao, *J. Am. Chem. Soc.*, 2008, **130**, 28.
- 15 Y. Huang, Z. Xu, Y. Yang, T. Tang, R. Huang and J. Shen, *J. Phys. Chem. C*, 2009, **113**, 6533.
- 16 V. Dravid, J. Host, M. Teng, B. Elliott, J. Hwang, D. Johnson, T. Mason and J. Weertman, *Nature*, 1995, **374**, 602.
- 17 X. C. Sun and X. L. Dong, *Mater. Res. Bull.*, 2002, **37**, 991.
- 18 J. H. Hwang, V. P. Dravid, M. H. Teng, J. J. Host, B. R. Elliott, D. L. Johnson and T. O. Mason, *J. Mater. Res.*, 1997, **12**, 1076.
- 19 A. A. E. Gendy, E. M. M. Ibrahim, V. O. Khavrus, Y. Krupskaya, S. Hampel, A. Leonhardt, B. Buechner and R. Klingeler, *Carbon*, 2009, **47**, 2821.
- 20 J. Jiao, S. Seraphin, X. K. Wang and J. C. Withers, *J. Appl. Phys.*, 1996, **80**, 103.
- 21 M. P. Fernandez-Garcia, P. Gorria, M. Sevilla, M. P. Proenca, R. Boada, J. Chaboy, A. B. Fuertes and J. A. Blanco, *J. Phys. Chem. C*, 2011, **115**, 5294.
- 22 V. Tzitzios, G. Basina, M. Gjoka, V. Alexandrakis, V. Georgakilas, D. Niarchos, N. Boukos and D. Petridis, *Nanotechnology*, 2006, **17**, 3750.
- 23 Y. P. Sun, H. W. Rollins and R. Guduru, *Chem. Mat.*, 1999, **11**, 7.
- 24 M. Brust, M. Walker, D. Bethell, D. Schiffrin and R. Whyman, *J. Chem. Soc., Chem. Commun.*, 1994, **7**, 801.
- 25 O. Cintora-Gonzalez, C. Estournes, M. Richard-Plouet and J. L. Guille, *Mater. Sci. Eng., C*, 2001, **15**, 179.
- 26 Y. W. Duan and J. G. Li, *Mater. Chem. Phys.*, 2004, **87**, 452.
- 27 D. L. Tao and F. Wei, *Mater. Lett.*, 2004, **58**, 3226.
- 28 F. C. Fonseca, G. F. Goya, R. F. Jardim, R. Muccillo, N. L. V. Carreno, E. Longo and E. R. Leite, *Phys. Rev. B*, 2002, **66**, 104406.
- 29 S. Che, K. Takada and N. Mizutani, *J. Mater. Sci. Lett.*, 1998, **17**, 1227.
- 30 T. Seto, K. Koga, H. Akinaga, F. Takano, K. Sakiyama, M. Hirasawa and T. Orii, *Appl. Phys. A*, 2004, **79**, 1165.
- 31 E. M. Gonzalez, M. I. Montero, F. Cebollada, C. de Julian, J. L. Vicent and J. M. Gonzalez, *Europhys. Lett.*, 1998, **42**, 91.
- 32 J. Nogues, V. Langlais, J. Sort, S. Doppiu, S. Surinach and M. D. Baro, *J. Nanosci. Nanotechnol.*, 2008, **8**, 2923.
- 33 L. D. Bianco, F. Boscherini, A. L. Fiorini, M. Tamisari, F. Spizzo, M. V. Antisari and E. Piscopiello, *Phys. Rev. B*, 2008, **77**, 094408.
- 34 E. Winkler, R. D. Zysler, M. V. Mansilla, D. Fiorani, D. Rinaldi, M. Vasilekaki and K. N. Trohidou, *Nanotechnology*, 2008, **19**, 185702.
- 35 B. Martinez, X. Obradors, L. Balcells, A. Rouanet and C. Monty, *Phys. Rev. Lett.*, 1998, **80**, 181.
- 36 N. Rinaldi-Montes, P. Gorria, D. Martinez-Blanco, A. B. Fuertes, L. F. Barquin, J. R. Fernandez, I. de Pedro, M. L. F. Gubieda, J. Alonso, L. Olivi, G. Aquilanti and J. A. Blanco, *Nanoscale*, 2014, **6**, 457.
- 37 R. H. Kodama, S. A. Makhlof and A. E. Berkowitz, *Phys. Rev. Lett.*, 1997, **79**, 1393.
- 38 J. Nogues and I. K. Schuller, *J. Magn. Magn. Mater.*, 1999, **192**, 203.
- 39 J. Nogues, J. Sort, V. Langlais, V. Skumryev, S. Surinach, J. S. Munoz and M. D. Baro, *Phys. Rep.*, 2005, **422**, 65.
- 40 M. Estrader, A. Lopez-Ortega, S. Estrade, I. V. Golosovsky, G. Salazar-Alvarez, M. Vasilakaki, K. N. Trohidou, M. Varela, D. C. Stanley, M. Sinko, M. J. Pechan, D. J. Keavney, F. Peiro, S. Surinach, M. D. Baro and J. Nogues, *Nat. Commun.*, 2013, **4**, 2960.
- 41 O. Metin, V. Mazumder, S. Ozkar and S. Sun, *J. Am. Chem. Soc.*, 2010, **132**, 1468.
- 42 H. Guo, Y. Chen, X. Chen, R. Wen, G. H. Yue and D. L. Peng, *Nanotechnology*, 2011, **22**, 195604.
- 43 P. Gorria, M. Sevilla, J. A. Blanco and A. B. Fuertes, *Carbon*, 2006, **44**, 1954.
- 44 P. Gorria, M. P. Fernandez-Garcia, M. Sevilla, J. A. Blanco and A. B. Fuertes, *Phys. Status Solidi RRL*, 2009, **3**, 4.
- 45 A. C. Johnston-Peck, J. Wang and J. B. Tracy, *ACS Nano*, 2009, **3**, 1077.
- 46 J. Curiale, M. Granada, H. E. Troiani, R. D. Sanchez, A. G. Leyva, P. Levy and K. Samwer, *Appl. Phys. Lett.*, 2009, **95**, 043106.
- 47 J. van Driel, F. R. de Boer, R. Coehoorn, G. H. Rietjens and E. S. J. Heuvelmans-Wijdenes, *Phys. Rev. B*, 2000, **61**, 15321.
- 48 P. Voorhees, *J. Stat. Phys.*, 1985, **38**, 231.
- 49 R. A. Sperling, P. R. Gil, F. Zhang, M. Zanella and W. J. Parak, *Chem. Soc. Rev.*, 2008, **37**, 1896.
- 50 J. Rodriguez-Carvajal, *Satellite Meeting on Powder Diffraction of the XV IUCr Congress*, 1990, 127.
- 51 D. Martinez-Blanco, P. Gorria, J. A. Blanco, M. J. Perez and J. Campo, *J. Phys.: Condens. Matter*, 2008, **20**, 335213.
- 52 B. Ravel and M. Newville, *J. Synchrotr. Radiat.*, 2005, **12**, 537.
- 53 S. Sasaki, K. Fujino and Y. Takeuchi, *Proc. Jpn. Acad. Ser. B-Phys. Biol. Sci.*, 1979, **55**, 43.
- 54 S. Helveg, C. Lopez-Cartes, J. Sehested, P. L. Hansen, B. S. Clausen, J. R. Rostrup-Nielsen, F. Abild-Pedersen and J. K. Nørskov, *Nature*, 2004, **427**, 426.
- 55 S. Hofmann, R. Sharma, C. Ducati, G. Du, C. Mattevi, C. Cepek, M. Cantoro, S. Pisana, A. Parvez, F. Cervantes-Sodi, A. C. Ferrari, R. Dunin-Borkowski, S. Lizzit, L. Petaccia, A. Goldoni and J. Robertson, *Nano Lett.*, 2007, **7**, 602.
- 56 J. B. Yi, J. Ding, Y. P. Feng, G. W. Peng, G. M. Chow, Y. Kawazoe, B. H. Liu, J. H. Yin and S. Thongmee, *Phys. Rev. B*, 2007, **76**, 224402.
- 57 S. D. Tiwari and K. P. Rajeev, *Phys. Rev. B*, 2005, **72**, 104433.
- 58 H. Khurshid, M. H. Phan, P. Mukherjee and H. Srikanth, *Appl. Phys. Lett.*, 2014, **104**, 072407.
- 59 J. Crangle and G. Goodman, *Proc. Roy. Soc. Lond. A.*, 1971, **321**, 477.
- 60 A. Tamion, M. Hillenkamp, F. Tournus, E. Bonet and V. Dupuis, *Appl. Phys. Lett.*, 2009, **95**, 062503.
- 61 S. Guo, W. Liu, H. Meng, X. H. Liu, W. J. Gong, Z. Han and Z. D. Zhang, *J. Alloys Compd.*, 201, **497**, 10.
- 62 M. Ali, P. Adie, C. H. Marrows, D. Greig, B. J. Hickey and R. L. Stamps, *Nat. Mater.*, 2007, **6**, 70.
- 63 Y. Tang, Y. Sun and Z. Cheng, *J. Appl. Phys.*, 2006, **100**, 023914.